Monthly Notices of the ROYAL ASTRONOMICAL SOCIETY

MNRAS **498,** 2766–2777 (2020) doi:10.1093/mnras/staa2508
Advance Access publication 2020 August 19

A recent major merger tale for the closest giant elliptical galaxy Centaurus A

Jianling Wang,[1]★ Francois Hammer,[2] Marina Rejkuba,[3] Denija Crnojević[4] and Yanbin Yang[2]

[1]*CAS Key Laboratory of Optical Astronomy, National Astronomical Observatories, Beijing 100101, China*
[2]*GEPI, Observatoire de Paris, CNRS, Place Jules Janssen, F-92195 Meudon, France*
[3]*European Southern Observatory, Karl-Schwarzschild-Straße 2, D-85748 Garching bei München, Germany*
[4]*University of Tampa, 401 West Kennedy Boulevard, Tampa, FL 33606, USA*

Accepted 2020 August 14. Received 2020 August 13; in original form 2020 June 26

ABSTRACT

We have used hydrodynamical simulations to model the formation of the closest giant elliptical galaxy Centaurus A. We find that a single major merger event with a mass ratio of up to 1.5, and which has happened ∼2 Gyr ago, is able to reproduce many of its properties, including galaxy kinematics, the inner gas disc, stellar halo ages and metallicities, and numerous faint features observed in the halo. The elongated halo shape is mostly made of progenitor residuals deposited by the merger, which also contribute to stellar shells observed in the Centaurus A halo. The current model also reproduces the measured planetary nebula line-of-sight velocity and their velocity dispersion. Models with a small mass ratio and relatively low gas fraction result in a de Vaucouleurs profile distribution, which is consistent with observations and model expectations. A recent merger left imprints in the age distribution that are consistent with the young stellar and globular cluster populations (2–4 Gyr) found within the halo. We conclude that even if not all properties of Centaurus A have been accurately reproduced, a recent major merger has likely occurred to form the Centaurus A galaxy as we observe it at present day.

Key words: Galaxies: evolution – galaxies: formation – Galaxies: interactions.

1 INTRODUCTION

Understanding the star formation history and mass assembly history of galaxies is one of the most challenging tasks in modern astrophysics. Elliptical galaxies are the most massive ones in the classification of Hubble (Hubble 1936). They contain ∼22 per cent of the total mass in stars in the local universe and this fraction goes to 75 per cent for spheroids, including S0 and spiral bulges. The massive early-type galaxies (ETGs) are believed to form according to a two-phase scenario (e.g. Daddi et al. 2005; Oser et al. 2010; Arnold et al. 2011; Iodice et al. 2017; Naab & Ostriker 2017; Pulsoni et al. 2020). At high redshifts, gas collapses in the centre of dark matter and intense star formation occurs, to be subsequently quickly quenched. Then in a second stage, the accretion is dominant and ETGs grow efficiently in size through a series of mergers. The complex formation process through mergers and accretion of nearby galaxies makes it difficult to disentangle mixed material and stars originating from different progenitors.

Centaurus A (Cen A, NGC 5128), the central galaxy of the Centaurus group, is the closest easily observable giant elliptical galaxy with a distance of 3.8 Mpc (Harris, Rejkuba & Harris 2010). The iconic optical image of Cen A with a prominent twisted dust lane traversing a large spheroid has led to galaxy classification as peculiar elliptical or sometimes also S0 or S0p (see Harris 2010, for more details about Cen A's classification). This morphology has been ascribed already in the 50-ies to a possible merger origin. Baade & Minkowski (1954) interpreted the object as consisting of two nebulae, an elliptical nebula and a second system, possibly a spiral, that are *'in a state of strong gravitational interaction, perhaps actually in collision'*. A number of studies have pointed out that the main body of the galaxy has a light distribution of a 'normal' elliptical following closely the de Vaucouleur's $r^{1/4}$ profile (Sersic 1958; van den Bergh 1976; Dufour et al. 1979), and that the denomination as peculiar was perhaps undeserving and only a result of the proximity, which offers more detailed observations than possible in more distant systems (Ebneter & Balick 1983; Harris 2010). The proximity of Cen A provides excellent opportunities to study the galaxy in exquisite detail, and a possibility to disentangle its formation history.

Wang et al. (2012, 2015) and Hammer et al. (2010, 2018) modelled the formation of nearby giant spirals using numerical simulations of major mergers of two gas-rich spiral galaxies. Such a code can be adapted to explore a possibility of reproducing the observed properties of Cen A as a result of a major merger. Through comparison of observational properties of Cen A with those predicted by merger simulations, we can learn about galaxy formation processes.

In spite of already mentioned ideas about the merger origin of Cen A, some of its properties are suggesting an early rapid formation with subsequent evolution that included accretion(s) of satellite galaxies. This is in particular supported by the observed age distribution of stars (Rejkuba et al. 2005, 2011) and globular clusters (GCs) (Kaviraj et al. 2005; Woodley et al. 2007, 2010b; Beasley et al. 2008) that contain a bulk of the population that formed >10 Gyr ago, and up to 20–30 per cent that formed later having ages as young as ∼2–4 Gyr. Beasley et al. (2003) have compared the stellar halo and GC metallicity distribution functions (MDFs) with predictions of a cold dark matter (CDM) semi-analytic galaxy formation model, finding that the vast majority of star formation in the model

E-mail: wjianl@bao.ac.cn

occurs quiescently, while the red metal-rich GCs require hierarchical mergers, leading to predictions for their age–metallicity distribution. The warped disc that crosses the centre of Cen A and the presence of H I and CO in the disc and in shells surrounding the galaxy have been interpreted as coming from a relatively recent minor merger with a gas-rich spiral akin in size to M33 (Quillen et al. 1992; Mirabel et al. 1999; Charmandaris, Combes & van der Hulst 2000).

The formation scenario in which Cen A has experienced a relatively recent major merger has been invoked in the literature due to its perturbed morphology with the central dust lane, filaments, and shells, and it could perhaps also explain the presence of the active galactic nucleus in its centre (see the review by Israel 1998, for a historical perspective and further references). Peng, Ford & Freeman (2004a) suggested that the GC system and planetary nebulae (PNe) data in Cen A support a scenario according to which the main body of the galaxy was formed several Gyr ago through a dissipational merger of two unequal-mass disc galaxies and continued to grow through accretion of further satellites. Mathieu, Dejonghe & Hui (1996) built a triaxial dynamical model interpreting the Cen A PN kinematics measured by Hui et al. (1995) as the results of a major merger with a 3:1 mass ratio. Numerical simulations in which an elliptical galaxy is formed through a major merger of spiral galaxies have been made by Bekki, Harris & Harris (2003) as well as by Bekki & Peng (2006). They were used to explain the halo metallicity distribution and PN kinematics, respectively. Additional simulations that include gas dissipation and star formation are necessary to make further progress (Peng, Ford & Freeman 2004b). It has been shown that realistic mergers require a correct treatment of the gas through hydrodynamical simulations, and by using consistent hydrodynamical solvers (see Hopkins 2015, and references therein).

Hammer et al. (2013) proposed that the vast thin disc of satellites around our closest giant spiral M31 (Ibata et al. 2013) could be linked to a major merger. The model of M31 (Hammer et al. 2018) as a recent 2–3 Gyr old major merger reproduced successfully the giant stream and halo substructures in M31 (Ibata et al. 2007). This prompts the question of whether a similar explanation could be applied also to Cen A.

The aim of this paper is to verify if a numerical simulation of a major merger could explain several observational properties in Cen A. In Section 2, we describe data used for comparison with the models. The simulation method and initial conditions are described in Section 3. Results including comparisons to observations are presented in Section 4. In the last section, we discuss and summarize our results.

2 THE PROPERTIES OF CENTAURUS A

Centaurus A is one of the nearest and largest radio galaxies, and its optical counterpart is the giant elliptical galaxy NGC 5128 with the total integrated magnitude of $M_B = -21.2$ mag (Dufour et al. 1979). Throughout the paper, while we examine mostly the optical properties of the elliptical galaxy, we use its radio source name abbreviated to Cen A. Based on a review of distance measurements, Harris et al. (2010) derived the best-estimate distance for NGC 5128 of 3.8 ± 0.1 Mpc.[1] The integrated light measurements in the inner parts of the galaxy revealed a luminosity distribution similar to that of an E2 galaxy type following a de Vaucouleur's law over the range $20 < \mu_B < 25$ mag arcsec^{-2} and having an effective radius of $R_{\rm eff} =$ 305 arcsec measured in the B band (Dufour et al. 1979). At the distance of 3.8 Mpc, this implies $R_{\rm eff} = 5.6$ kpc.

Fall & Romanowsky (2018) have derived the stellar mass of Cen A based on the observed $B - V$ colours and the predicted relation between M/L_K and $B - V$ from stellar population models, assuming $M/L_K = 0.8$. The K-band luminosity from Two Micron All Sky Survey (Skrutskie et al. 2006) has been corrected for the bias that underestimates luminosity for large galaxies by their 'aperture corrections' (Romanowsky & Fall 2012). After rescaling the distance to 3.8 Mpc and the initial mass function (IMF) to a Salpeter 'diet', the total stellar mass is estimated to be $\sim 2 \times 10^{11}$ M$_\odot$.

The total dynamical mass has been measured using GCs, PN, H I gas, X-ray emission, and satellites. While these tracers cover different distances, the total mass is between 2.2×10^{11} M$_\odot$ at $\sim$15 kpc (Schiminovich et al. 1994; corrected to 3.8 Mpc distance) and 1.1×10^{12} M$_\odot$ at $\sim$80 kpc (Woodley et al. 2010a). Considering also dynamics of satellites, the mass of the whole Centaurus group is 9×10^{12} M$_\odot$ (Woodley 2006; Karachentsev et al. 2007). The M/L_B ratio is lower than that expected for an elliptical with values between 7 and 15 within inner 20 kpc and increasing outwards reaching $M/L_B = 52 \pm 22$ at 45 kpc in the halo and $M/L_B = 153 \pm 50$ for the Centaurus group (Kraft et al. 2003; Samurovic 2006; Woodley 2006).

The giant elliptical is traversed by a warped dust lane (Quillen et al. 2006) surrounded by a stellar ring populated by young red supergiant stars (Kainulainen et al. 2009), and it hosts a system of shells (Malin 1978; Peng et al. 2002) and an extended halo with numerous low-surface brightness streams (Crnojević et al. 2016).

Most of the gas in Cen A is located in a disc that follows the dust lane in the centre of the galaxy (Eckart et al. 1990; van Gorkom et al. 1990; Quillen et al. 1992; Espada et al. 2019). Furthermore, H I and molecular gas have also been detected extending out to about 15 kpc in the halo of Cen A (Schiminovich et al. 1994; Charmandaris et al. 2000; Oosterloo & Morganti 2005). H I in the central area is close to edge-on structure along the central dust lane that is roughly perpendicular to the jet, which is along PA=50° axis (Tingay et al. 1998). The central H I, CO, and dust are all part of a coherent warp that extends between 2 and 6500 pc (see Quillen et al. 2010, for a review). There are multiple folds in this warped disc. The northern radio lobe is likely pointing towards us, while the southern lobe points away. The gas and dust disc is mostly visible in the optical in the north-eastern part where it is in front of the galaxy, while in the south-western side it is partly obscured by the galaxy body (Morganti 2010; Struve et al. 2010).

The gas in the halo is distributed in a ring-like structure that rotates in the same direction as the main stellar body of the galaxy, and molecular gas is found to be located in close proximity of stellar shells (Charmandaris et al. 2000). In the north-eastern region of the H I ring, along the radio jet direction, there is evidence of recent star formation (Graham 1998; Mould et al. 2000; Rejkuba et al. 2001, 2002) possibly triggered by interaction of the jet with the interstellar medium (Oosterloo & Morganti 2005; Salomé et al. 2016b; Santoro et al. 2016). The total H I mass of 4.9×10^8 M$_\odot$ in the disc and another $\sim 5 \times 10^7$ M$_\odot$ in the shells were reported by Schiminovich et al. (1994) and Struve et al. (2010). A similar amount of molecular gas was found by Charmandaris et al. (2000), Wild & Eckart (2000), and Salomé et al. (2016a). The overall H I fraction in Cen A is relatively low for an ETG with $M_{\rm H\,I}/L_B = 0.01$ (Struve et al. 2010). Parkin et al. (2012) reported a total dust mass of $(1.59 \pm 0.05) \times 10^7$ M$_\odot$ and a total gas mass of $(2.7 \pm 0.2) \times 10^9$ M$_\odot$ based on Herschel and JCMT observations. Most recent high-sensitivity and high-spatial resolution maps of the central disc in Cen A made in CO

[1] At the 3.8 Mpc distance, 1 arcmin is equivalent to 1.1 kpc.

(1–0) with ALMA (Espada et al. 2019) found even larger reservoir of molecular gas amounting to 1.6×10^9 M .

Thanks to its proximity, the stellar halo of Cen A can be resolved into individual red giant branch (RGB) stars and from their colour distribution it is possible to measure an MDF, in addition to surface brightness distribution and mean metallicity gradient. The stellar MDF has been derived from optical photometry obtained with the *Hubble Space Telescope* (*HST*) in fields ranging in distance between 8 and 140 kpc (Harris, Harris & Poole 1999; Harris & Harris 2000, 2002; Rejkuba et al. 2005, 2014) from the centre of Cen A. Stellar halo age distribution was derived from the deepest *HST* field located ∼40 kpc south of the centre of the Cen A. Two burst models with 70–80 per cent of the stars forming in a short burst 12 ± 1 Gyr ago, and the 20–30 per cent of the stars forming 2–4 Gyr ago, provided the best fit to these observations (Rejkuba et al. 2011). This age distribution is consistent with the GC age distribution based on $U - B$ photometry (Kaviraj et al. 2005) and low-resolution spectroscopy (Peng et al. 2004a; Beasley et al. 2008; Woodley et al. 2010b). Wider area imagers, VIMOS on the VLT and Megacam on the Magellan telescope, were used to trace the surface density and metallicity gradients in the outer halo (Crnojević et al. 2013, 2016; Bird et al. 2015). The resolved stellar halo studies showed a relatively shallow metallicity gradient with a slope of $[\mathrm{M/H}]/\ R = -0.0054 \pm 0.0006$ dex kpc^{-1}, or $[\mathrm{M/H}]/\ R_{\mathrm{eff}} = -0.030 \pm 0.003$ dex per R_{eff} (Rejkuba et al. 2014). This may indicate that bulk of the halo was not assembled through accretion of many low-mass satellites, but rather from few massive ones.

Over 1000 PNe (Hui et al. 1995; Peng et al. 2004b; Walsh, Rejkuba & Walton 2015) and almost 600 GCs (Peng et al. 2004a; Beasley et al. 2008; Woodley et al. 2010a) have measured velocities providing kinematic information from centre out to $\sim 10 R_{\mathrm{eff}}$, with a few confirmed clusters and PNe as far out as $15.5 R_{\mathrm{eff}}$ or 85 kpc (Walsh et al. 2015), and many more cluster candidates out to 150 kpc (Taylor et al. 2017; Voggel et al. 2020). The halo of Cen A shows a disc-like feature, which has a large rotation along the major axis flattening at 100 km s^{-1} as traced by PN (Peng et al. 2004b). The zero-velocity contour of the velocity field is perpendicular to the stellar major axis with a pronounced twist. GCs show different kinematics between metal-poor and metal-rich components (Peng et al. 2004a; Woodley et al. 2010a). The metal-poor GCs are supported by dispersion (149 ± 4 km s^{-1}) with a flat dispersion profile extending to 20 arcmin and then possibly increasing outwards. The metal-rich GCs have a similar velocity dispersion, but they also exhibit a rotation of 43 ± 15 km s^{-1} around the isophotal major axis. The GC kinematics was discussed both as providing evidence supporting (Peng et al. 2004a) and against (Woodley et al. 2010a) a recent major merger formation scenario for the galaxy.

The studies mentioned above are mainly focusing on the large scale properties of the Cen A halo and its stellar population content and dynamics. The properties and studies of the radio jet and black hole in the centre region are beyond the scope of our analysis, and are not discussed in this paper.

3 NUMERICAL SIMULATIONS AND INITIAL CONDITIONS

The numerical simulations were carried out with the GIZMO code (Hopkins 2015), which is based on a new Lagrangian method for hydrodynamics, and has simultaneously properties of both smoothed particle hydrodynamics and grid-based/adaptive mesh refinement methods. We have implemented into GIZMO star formation and feedback processes as described in Wang et al. (2012) following the method of Cox et al. (2006). The cooling process has been implemented in GIZMO with an updated version of Katz, Weinberg & Hernquist (1996). This code has been used in simulating the formation of Magellanic Stream (Wang et al. 2019).

The initial conditions were set up following the procedure of Wang et al. (2012, 2015) and Hammer et al. (2010, 2018), who modelled the formation of a nearby giant spiral after a major merger of two gas-rich spirals. Since Cen A is an ETG with low gas fraction, progenitors with moderate gas fractions (20–40 per cent) are used, which leads to a larger bulge fraction for the merger remnant (Hopkins et al. 2009, 2010). Moreover, Sauvaget et al. (2018) experimented with a series of major mergers showing that only those with an initially low gas fraction and low mass ratio (<2) are able to produce giant elliptical remnants. All the simulations are performed assuming a baryon fraction of 9 per cent (Wang et al. 2012, 2015). The initial gas disc scale length is 2–3 times larger than that of the stellar disc, since observations show that gas discs are more extended than stellar discs (van der Kruit 2007).

There are several thin streams in the halo of Cen A that, if associated with a major merger, would favour a prograde orbit for one progenitor. Indeed, Toomre & Toomre (1972) showed that for prograde encounters (orbital angular momentum aligned with those of the initial disc galaxies), particles are more in resonance with the tidal field and result in far more prominent tidal tails than retrograde encounters (see also realizations of tidal tails by Wang et al. 2012, 2015). This also applies for interpreting the straight stream (Crnojević et al. 2016), which leads us to use a prograde orbit for one of the progenitors. We also use a polar orbit for the other progenitor, since Bekki & Peng (2006) found that a collision with a highly inclined orbital configuration can reproduce Cen A's kinematics (Peng et al. 2004b). Observations show ongoing star formation with ∼15 Myr old stars along the jet direction in the north-east halo extending up to ∼20 kpc (Graham 1998; Mould et al. 2000; Rejkuba et al. 2001). Additional ionized gas filaments are observed up to 35 kpc distance (Neff, Eilek & Owen 2015). However, beyond those relatively confined areas with ongoing low-efficiency star formation (Salomé et al. 2016b), the stellar age distribution within 40 kpc in the halo has a moderate (20–30 per cent) fraction of stars that formed as recently as 2 Gyr ago (Rejkuba et al. 2011). This epoch could indicate the fusion time of the merger (Hammer et al. 2018), during which some material can be easily ejected from the central regions. We compare the simulated merger remnants at the time that corresponds to 2 ± 1 Gyr after fusion with observations. The time-scale for the current major merger is longer than that for minor merger models. Quillen, Graham & Frogel (1993) proposed a time-scale of the order of 0.2 Gyr after accretion of a minor spiral to model the warp formation. This is also roughly consistent with the shell-like feature formation time-scale (Schiminovich et al. 1994; Peng et al. 2002). We developed an efficient software that enables three-dimensional visualization of results to model nearby galaxy formation. For further details about this software, we refer to Hammer et al. (2010, 2018) and Wang et al. (2012, 2015).

Following the same procedure as done in our previous studies (Hammer et al. 2010, 2018; Wang et al. 2012, 2015), we have optimized the parameter space, including the pericentre, two inclination angles for each progenitor, the initial gas fractions, and mass ratio. Given the large parameter space, It is impossible to examine all parameters in detail. However, the above constraints help reduce the parameter space significantly. During its exploration, we first build large coarse grid of parameters with values in the following ranges: (1) mass ratio of progenitors between 1 and 3, (2) the orbital parameters with pericentre distance between 5 and 40 kpc

Table 1. Parameters of the four models used in this study. The following parameters are listed in the table rows: (1) the mass ratio of progenitor galaxies; (2–5) the initial angles (in degrees) of the progenitors with respect to the orbital plane; (6 and 7) initial gas fraction for the primary and secondary progenitors; (8 and 9) initial scale length of the stellar components of each progenitor; (10 and 11) initial scale length of the gas component of each progenitor; (12) pericentre in kpc; (13) eccentricity orbital parameter; (14) the number of particles; (15) particle mass ratio; (16) softening length; (17) the time that best matches the observations after beginning the simulations; (18 and 19) Sérsic index and effective radius used to fit the surface mass density; (20) the final gas fraction; and (21) the final gas mass.

Parameters	Model-6	Model-7	Model-10	Model-11
Mass ratio	1.0	1.0	1.0	1.5
Gal1 incy	90	90	90	90
Gal1 incz	−90	−90	−90	−90
Gal2 incy	70	80	80	80
Gal2 incz	−40	−50	−50	−50
Gal1 gas fraction	0.2	0.2	0.2	0.2
Gal2 gas fraction	0.2	0.2	0.4	0.4
Gal1 h_{star} (kpc)	5.1	5.1	8.1	8.5
Gal2 h_{star} (kpc)	5.1	5.1	5.1	4.86
Gal1 h_{gas} (kpc)	10.2	10.2	16.2	17.0
Gal2 h_{gas} (kpc)	10.2	10.2	15.3	14.58
r_{peri} (kpc)	20	20	18	25
eccentricity	1.0	1.0	1.0	1.0
$N_{particle}$	1.85M	1.85M	1.85M	1.85M
m_{dm}:m_{star}:m_{gas}	4:1:1	4:1:1	4:1:2	4:1:1
Softening($_{dm}$:$_{star}$:$_{gas}$) (kpc)	0.3:0.1:0.1	0.3:0.1:0.1	0.3:0.1:0.1	0.3:0.1:0.1
Observed time (Gyr)	5.8	5.8	6.4	5.4
Sersic index (n)	4.7	4.4	6.2	4.4
Effective radius (kpc)	3.7	4.0	4.4	6.3
Final gas fraction	3.2 per cent	3.5 per cent	4.1 per cent	8.8 per cent
Gas mass ($r < 50$ kpc) (10^{10} M)	0.61	0.68	0.73	1.58

and eccentricity ranging from 0.9 to 1, and (3) different inclination angles of initial progenitors. Besides these, we also checked our major merger library that was built specifically for NGC 5907 and NGC 4013 (Wang et al. 2012, 2015) in order to further constrain the parameter space. Snapshots from each simulation have been examined using 0.1 Gyr time-steps. After finding possible candidate models, we fine-tune the parameters to optimize the simulation. A total of 220 simulations have been performed to provide the necessary material for reproducing Cen A's observed properties. A systematic comparison between these models and observations has let us to select four of them that show the best reproduction of Cen A's properties. Parameters of these four models are presented in Table 1. They all have similar angular orbital parameters as well as the initial gas fractions. Most of the variance is in mass ratio, initial scale lengths, and pericentres, all being major ingredients in merger modelling, which well demonstrate the final result variance from different models. We run simulations using 1.85 million particles per simulation. Additionally, we also run some simulations with 6 and 10 million particles. There was little change with the increased number of particles demonstrating convergence of our simulations.

In what follows, we compare several features from our simulations to the observed properties of Cen A to assess the robustness of our methods and results.

4 THE RESULTS

4.1 Galaxy morphology and faint features formed during merger

Fig. 1 shows the stellar mass distribution resulting from the four models and compares them to the observations made by Crnojević et al. (2016) and image from D. Malin published in Israel (1998). All models reproduce the main features observed in the Cen A imagery. In the deepest observations from Crnojević et al. (2016), the halo of Cen A shows an elongated shape along the major axis. At both ends of the major axis, there are several overdensities and clumps, in particular on the bottom side of the galaxy. This behaviour is well reproduced by our simulations and identified to be main residuals of the merger event. Interestingly, our simulations are able to reproduce one of the most stunning features in Cen A's halo, i.e. the long stream to the north-east of the galaxy, as a result of the central major merger. The stream was first discovered in the ground-based imaging presented by Crnojević et al. (2016) and further followed up with *HST* (Crnojević et al. 2019); it is 60 kpc long and located at a projected distance of 80 kpc from Cen A, and it features a clear remnant (dubbed Dw3) that hosts a candidate nuclear star cluster (Seth et al., in preparation). The stream could have originated from the tidal influence of Cen A on an $M_V \sim -15$ dwarf galaxy, leading to the observed S-shape of the stripped remnant's outer isophotes (Crnojević et al. 2016). However, the shape of Dw3's tidal tails, and in particular their straightness, is somewhat unusual: One possible interpretation is that this is the result of a recent accretion event, which is observed close to apocentre and with a large velocity component in the direction of the plane of the stream (S. Pearson, private communication). It is intriguing that this feature can be naturally obtained from our simulations: This could possibly imply that Dw3 has a tidal dwarf origin instead (Metz & Kroupa 2007; Fouquet et al. 2012; Kroupa, Pawlowski & Milgrom 2012; Hammer et al. 2013; Yang et al. 2014; Ploeckinger et al. 2015; Baumschlager et al. 2019). This scenario can be tested by obtaining kinematics of the remnant to assess the presence/absence of dark matter. We also highlight that one model (Model-10) reproduces as well a second, curved stream that can be seen on the left-hand side of

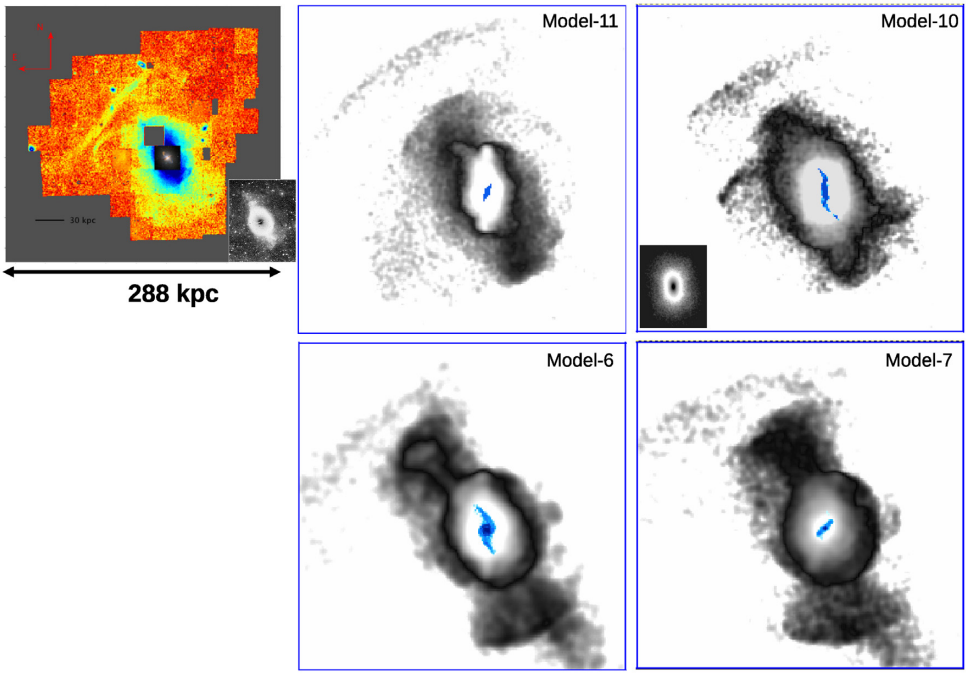

Figure 1. Comparison of observed (left) stellar mass distribution with simulations (middle and right-hand panels). Observational data on the top-left panel are from Crnojević et al. (2016). The observed stellar density map has been scaled in physical size consistent with the simulated Models. The small insert next to the observed map shows the image from D. Malin published in Israel (1998) for comparison with the Model-10 (see the insert in the top-right panel). Four simulation results are shown on the right-hand panels (see Table 1). For clarity, the colour in the centre of each model image has been inverted and overlapped. The final gas morphology has been superimposed with blue colour on each simulation image. The size of each simulated image is 350 by 350 kpc.

the images in the top-left (Crnojević et al. 2016) and top-right panels of Fig. 1.

Observations have revealed a warped H I gas disc (van Gorkom et al. 1990; Schiminovich et al. 1994; Israel 1998), which is roughly perpendicular to the major axis of the stellar component. In Fig. 1, the gas component is the blue component overlapping the centre of the galaxy. Three models show such an edge-on gas disc component, and two of them, namely Model-11 and Model-7, have gas disc position angles roughly consistent with observations. We notice, however, that the gas disc component presents large angular changes with time, which means that capturing the proper position angle is a difficult and lengthy task. To get a better match, more models are needed for fine-tuning.

Perhaps, the major weakness of our modelling is the overall size of Cen A, which is systematically larger in simulations than the observed one. For example, in Model-10 the distance from the galaxy centre to the faint features found in the bottom of the image is about 22 per cent larger than that observed, while Model-7 leads to even more overestimated size (60 per cent larger). Moreover, for Model-10 and Model-7, the projected distance from the galaxy centre to the straight stream is 70 and 100 per cent larger than that observed, respectively. Thus, our modelling is well indicative of the structures formed during the major merger that has occurred in Cen A, but does not represent an accurate reproduction of this galaxy, contrary to the one obtained in Hammer et al. (2018) for M31. We notice that to get such an accurate reproduction of M31 required performing close to 1000 different models, most of them being dedicated for fine-tuning. To recover the projected distance between the straight stream and the galaxy centre, different projected angles need to be considered. Alternatively, the mismatch could be due to the low baryon-to-dark matter ratio adopted here, since it possibly leads to a merger that is too energetic and expels too large quantities of material in the galaxy outskirts. Among several fine-tuning parameters that can be experimented with, one may consider changing the initial scales of the progenitors, as well as the merger pericentre.

The left-hand panels of Fig. 2 show how the stellar particles from the two progenitors are distributed. While both progenitors contribute to the central regions, there are clear differences in their outskirt distributions. For example, the straight stream is always coming from a single progenitor as well as the shell-like structures on both top and bottom sides of the galaxy (see red particles). The other progenitor (see green particles) may also contribute to the elongated distribution of the residuals along the major axis, though with large differences from one model to another.

The distance distribution of residuals in the galaxy outskirts is shown in the middle panels of Fig. 2. For Model-6, the straight stream is found 300 kpc behind Cen A. On the contrary, in Model-10 it is 100 kpc in front of Cen A. As shown by Crnojević et al. (2019, see their table 5), the distance estimates along this stream are not well constrained by observations, with values ranging from 150 kpc in front of Cen A to 750 kpc further away. Uncertainties from observations add another reason why fine-tuning of the model could not be accomplished, for the moment.

In the right-hand panels of Fig. 2, the colour coding indicates the standard deviation of the distances. In most cases, the standard deviation is around 60 kpc in the straight stream such as in Model-10, while it may reach 110 kpc in Model-6. The observed difference in distance at different positions along the straight stream is quite large, reaching up to 900 kpc in Crnojević et al. (2019) (between Dw3-WFC3 and Dw3S-ACS). This is significantly larger difference than the distance deviation in the models, and may indicate that the straight stream is made of different components and/or has a different origin, as discussed above.

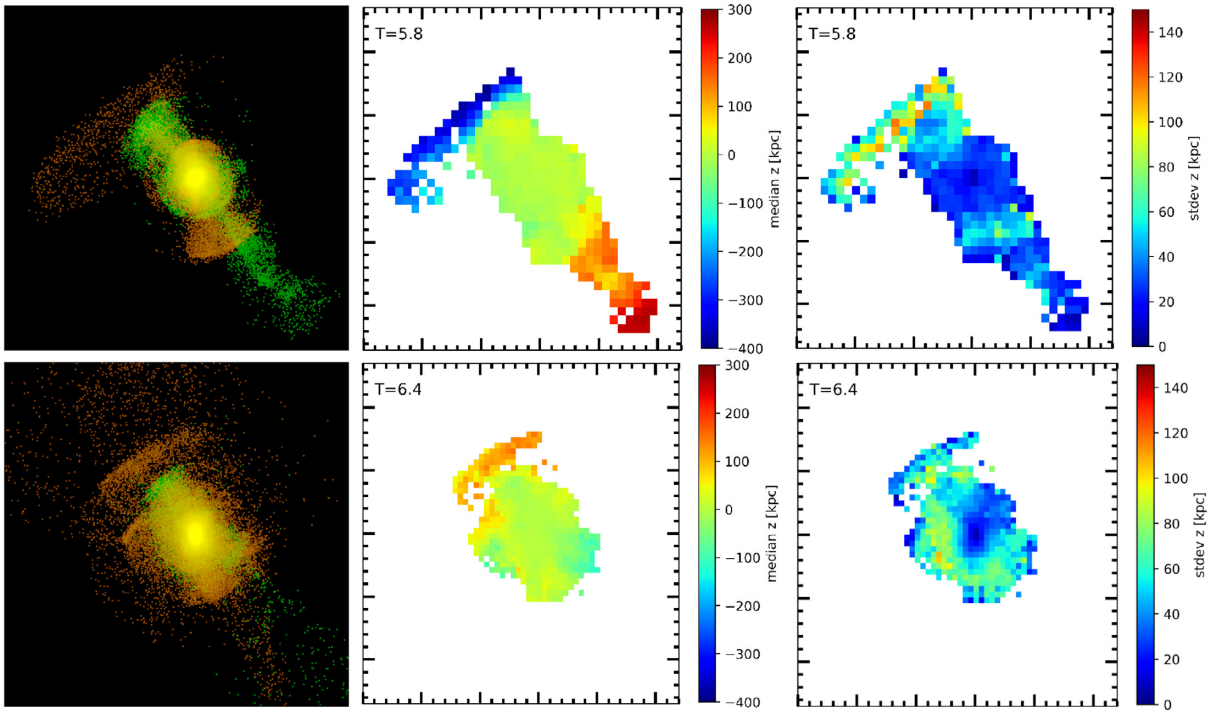

Figure 2. The left-hand panels show the particle distribution with red and green colours indicating each of the two progenitors, for Model-6 (top) and Model-10 (bottom), respectively. The middle panels indicate the stellar particles distance with respect to the centre of galaxy. The negative distance values are behind the galaxy and positive values are in front of the galaxy. The right-hand panels show the standard deviation of the distance distribution. The size of each panel is 540 by 540 kpc.

4.2 Velocity field

Over the last few decades, the kinematic properties of Cen A have been studied using different tracers, including spectroscopy of integrated stellar light (Wilkinson et al. 1986), of PN (Hui et al. 1995; Peng et al. 2004b), and of GCs (Peng et al. 2004a; Woodley et al. 2007, 2010a; Beasley et al. 2008). These studies provide valuable constraints on the kinematic properties of Cen A and total mass.

The bottom panels of Fig. 3 show the velocity field (left) and dispersion map (right) for Model-6. In this figure, the galaxy has been rotated to have the major axis along to the x-axis to ease the comparison with the observations by Peng et al. (2004b) shown in the top two panels. Peng et al. (2004b) used PN to study the velocity field. The final Model-6 remnant shows a rotation along the major axis with an amplitude of about 150 km s^{-1}, which is fully consistent with the observations (Peng et al. 2004b). The central peak in the velocity dispersion map reaches about 150 km s^{-1}, which is also consistent with observations (Peng et al. 2004b). Given the discrete tracer (PN), the observations show a sparser sampling than that of the models.

The line of zero velocity traced by Peng et al. (2004b) is both misaligned and twisted with respect to the photometric axes (Peng et al. 2004b). The simulated line of zero velocity shows similar features but with some geometrical differences.

4.3 Total mass distribution

Measurements of total mass of Cen A are important because they reveal the amount of dark matter. Several different methods and tracers have been used to estimate the total mass profile for Cen A. Their values, compiled from the literature and scaled to the galaxy distance of 3.8 Mpc, are plotted with different symbols and lines as shown on the right-hand side of Fig. 4. The total mass tracers include GCs (Woodley 2006; Woodley et al. 2007, 2010a), PN (Hui et al. 1995; Peng et al. 2004b; Samurovic 2006), H I gas (Graham 1979; van Gorkom et al. 1990; Schiminovich et al. 1994), and X-ray emission (Kraft et al. 2003). There is a significant scatter between the total mass measurements at comparable radii with a clear outward increase indicating that the galaxy is not dominated by dark matter in the inner $\sim 5R_{\rm eff}$ (see also Peng et al. 2004b, for further discussion). The red line (major merger) Model-6 simulation follows the outward increase in the total mass and lies in between observed data points.

4.4 Stellar mass profile

Dufour et al. (1979) have measured the surface brightness profile in the central region in the *B* band and obtained a very good fit with a de Vaucouleur's law. The extended surface brightness of Cen A to its outskirts has been measured using observations of individual RGB stars in the halo (Crnojević et al. 2013; Rejkuba et al. 2014; Bird et al. 2015). Crnojević et al. (2013) and Bird et al. (2015) resolved stellar halo of Cen A using VIMOS@VLT. Crnojević et al. (2013) observed two fields along the north-eastern major axis and another two fields along south-east minor axis, spanning a range of distances between ∼40 and 80 kpc. Bird et al. (2015) had a single VIMOS pointing at ∼65 kpc, but they combined their results with the RGB star counts and MDF measurements from previous *HST* data (Harris et al. 1999; Harris & Harris 2000, 2002; Rejkuba et al. 2005) to derive the density fall-off independently for metal-rich and metal-poor stars between ∼8 and 65 kpc. They found that both the metal-rich and metal-poor populations can be well fitted with a de Vaucouleur's law profile. Crnojević et al. (2013) noted a higher RGB number density along the major axis that deviated significantly

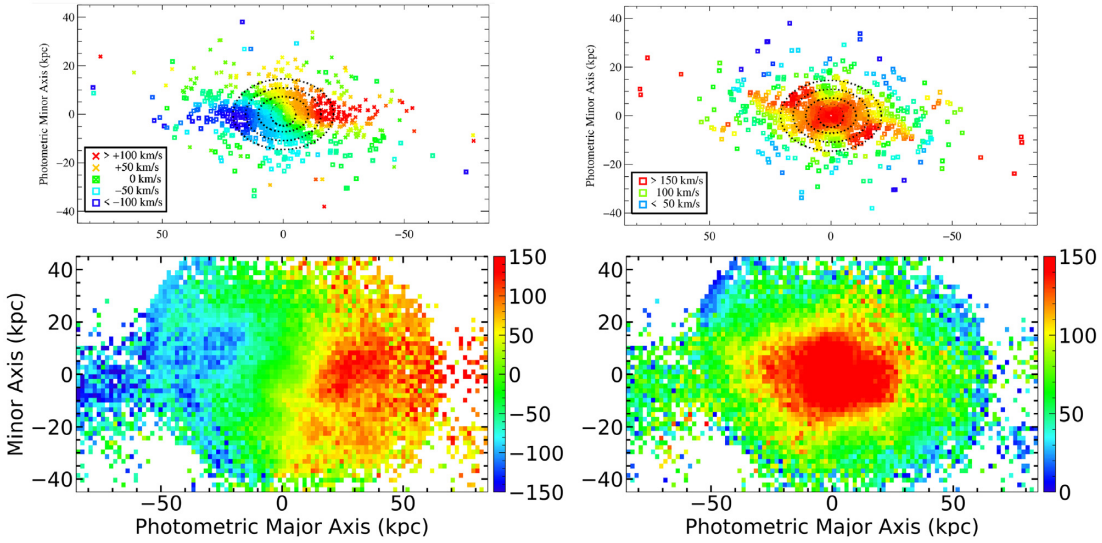

Figure 3. Comparison of the observed velocity field and velocity dispersion (top panels from Peng et al. 2004b measurements of PN) to that from Model-6 (bottom panels). Line-of-sight velocities are shown on the left, while the right column shows the associated velocity dispersion. The same colour map is used for observations and simulations.

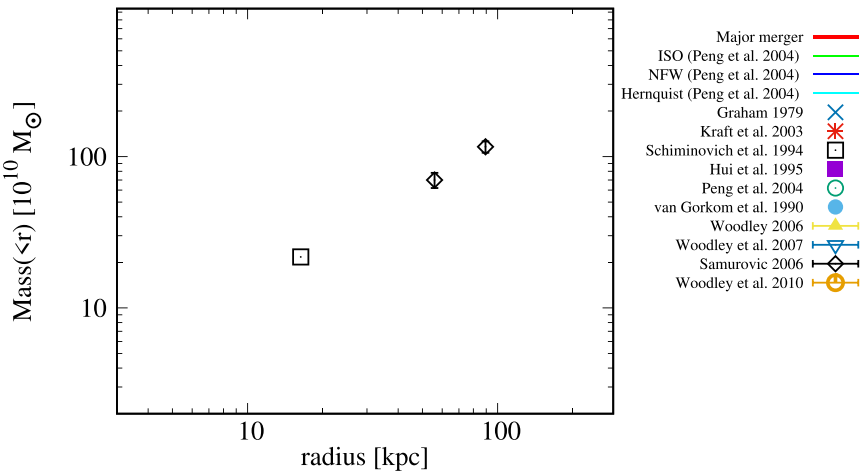

Figure 4. A comparison of total mass distribution of Model-6 (red solid line) to values from literature as listed on the right-hand side of the figure.

from a de Vaucouleur's profile beyond $R \geq 75$ kpc. Their data had insufficient coverage to distinguish between the genuine flattening of the radial profile and a presence of small-scale substructures in the halo. Rejkuba et al. (2014) used ACS and WFC3 cameras onboard the *HST* to extend resolved stellar halo studies out to a projected distance of 140 kpc along the galaxy major axis and 90 kpc along the minor axis. They found that in the outer halo, beyond $\sim 10 R_{\rm eff}$, there is a systematic increase in number counts along the major axis, even after accounting for field-to-field variations due to small-scale substructures. A de Vaucouleur's profile was shown to provide a good fit in the inner part of the galaxy as well as along the minor axis, while a power law provided a better fit along outer halo major axis.

Fig. 5 shows the surface mass density distribution of the Model-6 remnant, including its fit with a Sérsic profile. The Sérsic index is 4.7, which is consistent with the observed de Vaucouleur's profile ($n = 4$). For comparison, we plot in Fig. 5 the Dufour et al. (1979) *B*-band profile converted to stellar mass surface density. To convert the *B* surface brightness to a stellar mass surface density, we have used the $B - V$ colour versus stellar mass-to-light ratio relation (Bell et al. 2003). A $B - V$ colour of 0.84 is adopted from Dufour et al. (1979), and $V = 4.82$ from Bell & de Jong (2001).

The surface brightness distributions of RGB stars have been rescaled to that of Dufour et al. (1979). In this figure, we also compare the simulation with the surface brightness profile of RGB stars from Bird et al. (2015). In cyan, we show the power-law fit to RGB stars surface distribution from Rejkuba et al. (2014) rescaled to surface mass density as above. The excess of light in the outermost bins of the simulated mass surface density is well matched with this power law. The slope of the surface brightness and the stellar surface number counts can be robustly used for comparison to the model, because we are confident that the total stellar mass used in the models is well consistent with observations (see Section 4.3). The observed surface brightness profiles from integrated light and RGB star counts are consistent with profiles of the four merger remnants examined here, for which the Sérsic index ranges from 4.4 to 6.2, i.e. slightly larger than observations. Indeed, the profile from Dufour et al. (1979) is slightly shallower (Fig. 5). This could be either due to IMF variations

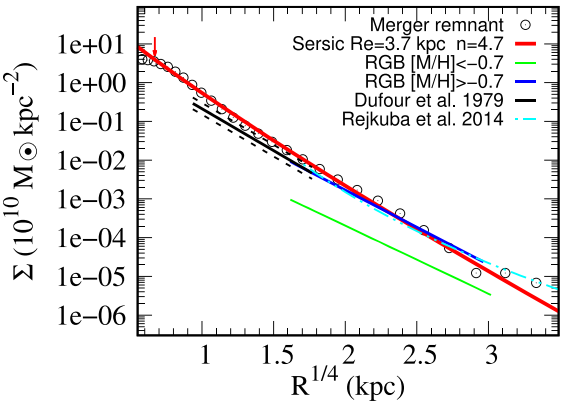

Figure 5. A comparison of the stellar mass distribution derived from observations with that of Model-6, which is fitted with a Sérsic profile (red line; see the parameters indicated on the top right). The red arrow indicates the two times softening length within which model predictions are limited by resolution. Fitting parameters for all of the four models are shown in Table 1. The observed surface brightness profile from Dufour et al. (1979) converted to stellar mass surface density (see the text) is shown with black solid line and the black dashed lines indicate the effect of a 0.15 dex systematic offset due to IMF variations. The observed surface brightness of RGB stars from Bird et al. (2015) is scaled to be consistent with that of Dufour et al. (1979) and shown with blue and green lines for metal-rich and metal-poor population, respectively. The cyan line shows the power-law distribution of light measured from RGB star counts from Rejkuba et al. (2014), which was motivated by excess of light along the major axis for fields beyond ∼50 kpc.

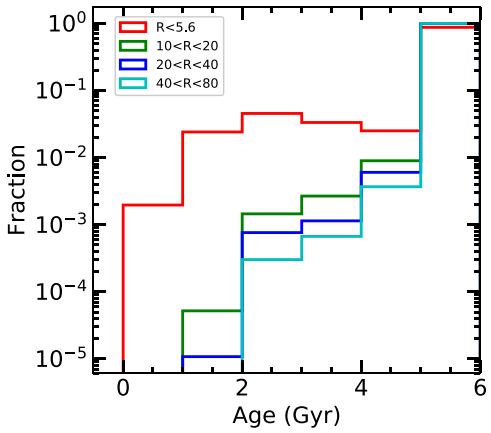

Figure 6. The stellar age distribution for stars at different radii based on Model-6. As the simulation started 6 Gyr ago, the peak at 6 Gyr is artificial and represents stars with a minimum age of 6 Gyr. Within 5.6 kpc, there is a peak around 2 Gyr, which likely indicates the fusion epoch during which star formation occurred in a central starburst (see e.g. Hammer et al. 2018).

(see black dashed lines showing a 0.15 dex systematic offset) or due to an increasing extinction in the central region.

The half-light radius of Cen A is changing with wavelength. Dufour et al. (1979) estimated it in the *B* band to be 305 arcsec (5.6 kpc) with a de Vaucouleurs profile. The half-mass radii for the four models are ranging from 3.7 to 6.3 kpc as shown in Table 1.

4.5 Star formation during the major merger

In Fig. 6, the age distribution of stars at different radii is shown. However, since the simulation is started 6 Gyr ago, the peak at 6 Gyr is artificial and indeed represents stars with ages larger or equal to 6 Gyr. This could have been corrected by resampling the age of these stars according to the observational constraints, though such considerations are out of the scope of this paper.

Rejkuba et al. (2011) found that the halo contains 20–30 per cent of stars that have been formed 2–4 Gyr ago in a field located ∼40 kpc south of the galaxy centre, which is also consistent with the age distribution of global clusters (Woodley et al. 2007, 2010b). The latter studies found many young GCs in the halo, with youngest ages around 2 Gyr, which confirms our choice of a recent fusion epoch. The above results are consistently reproduced by our modelling (see Fig. 6) after considering radii ranging from 10 to 80 kpc. A larger fraction of recent star formation is expected in the central regions (within the half-mass radius, $R_{\rm eff} = 5.6$ kpc) after a major merger, during which interaction between progenitors and then fusion have enhanced gas compression and favoured its transformation into stars.

4.6 Metallicity distribution and radial metallicity gradient

Thanks to the proximity of Cen A, its metallicity content can be measured from resolved stars. MDFs of halo stars in Cen A have been determined from the *HST* photometry (Harris et al. 1999; Harris & Harris 2000, 2002) in three fields at projected distances of 8, 21, and 31 kpc from the galaxy centre. They can be used to constrain the merger history of Cen A. Following Bekki et al. (2003), we have compared the MDF of Model-6 with observed MDFs. For the inner halo region field (8 kpc), we have selected stars with projected distance to the centre between 7 and 9 kpc. For comparison to the two outer halo fields (21 and 31 kpc), we have selected stars in the models with projected distance between 20 and 30 kpc. For the initial metallicity distribution in the progenitors, we have assumed

$$[\mathrm{M/H}] = [\mathrm{M/H}]_{R=0} + \alpha \times R.$$

The initial metallicity gradient α for the progenitors is -0.052 dex kpc^{-1}, which is from the results of MW open cluster from APOGEE and GALAH and consistent with the literature value ranging from -0.035 to -0.1 dex kpc^{-1} (Friel 1995; Carrera et al. 2019). The central metallicity value $[\mathrm{M/H}]_{R=0}$ is set to $+0.5$, which is very close to the maximum metallicity of MW bulge (Sarajedini & Jablonka 2005; Zoccali et al. 2017). This value is slightly lower than the maximum metallicity of M31 bulge, which is around $+0.9$ (see fig. 6 of Sarajedini & Jablonka 2005).

Fig. 7 compares the MDF for the inner halo field (8 kpc), and for the outer halo (21 and 31 fields). As pointed out by Rejkuba et al. (2014), the metallicity calibration in Harris et al. (1999) and Harris & Harris (2000, 2002) has an offset of 0.2 dex with respect to that in Rejkuba et al. (2014) due to use of different stellar evolutionary models. Also, there is a relatively large incompleteness correction at the high-metallicity end. Therefore, we have artificially shifted the black line (observed MDFs) in Fig. 7 by $+0.2$ dex. The median of observed MDFs is still lower than the model for both inner field and out field. These may reflect the incompleteness in photometry for the most metal-rich, reddest and faintest stars.

In Fig. 8, we compare the observed metallicity distribution along the radial direction with that from our model. Within 100 kpc, the model will fit the observation data. At 150 kpc, the metallicity is about 0.2 dex higher than that from observation, which may need more observation at that scale to overcome the variance from field to field.

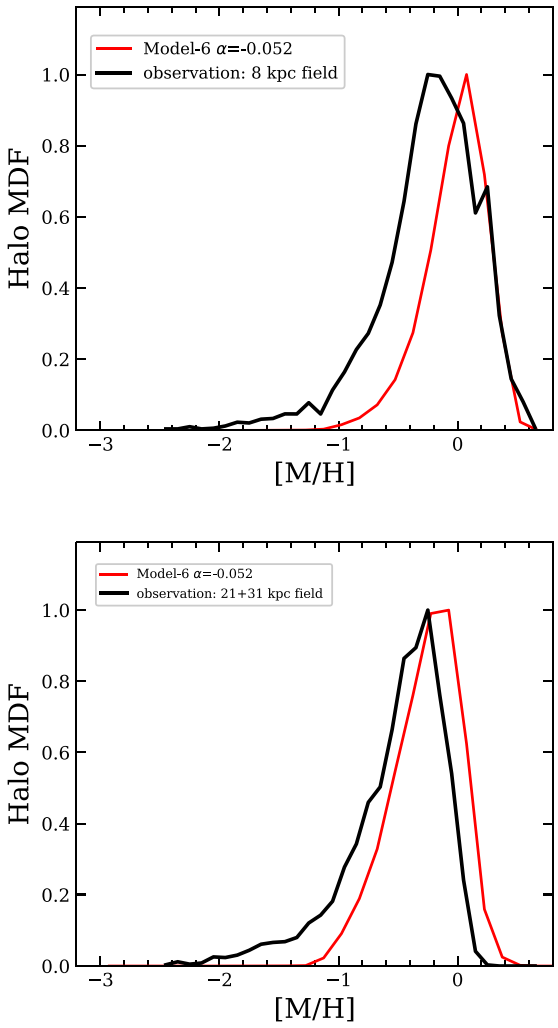

Figure 7. MDF compared with observations (Harris et al. 1999; Harris & Harris 2000, 2002). *Top panel:* field with a projected distance of 8 kpc to centre of Cen A. *Bottom panel:* field with a projected distance of 20–30 kpc to the centre of Cen A. To extract stellar metallicity from the models, we have used initial metallicity gradients for the progenitors, one with $\alpha = -0.052$ (see the red lines).

4.7 Ongoing star formation in the disc

There is still residual gas and star formation in the very centre of Cen A as visible in Fig. 1 both from observations (gas fraction of ∼1 per cent) and modelling (3.2–8.8 per cent from Table 1). This is linked to the central warped H I disc. Both young stars, Wolf–Rayet stars, and red supergiants and H II regions have been detected around the dusty disc (Graham 1979; Moellenhoff 1979; Minniti et al. 2004; Kainulainen et al. 2009). The star-forming warped disc is also well traced by the *Spitzer* IRAC map at 8 μm (Quillen et al. 2006, 2008), which is well known to trace the star formation (Wu et al. 2005). Furthermore, there is a reservoir of molecular gas fuelling low-level star formation (Eckart et al. 1990; Espada et al. 2019). Possible discrepancy in gas fraction between observations and simulations could be solved by implementing a less efficient feedback in the modelling to better exhaust the H I gas.

Fig. 9 shows the map of star formation rate (SFR) for Model-11 (top) and Model-6 (bottom) simulations. The ongoing star formation confined to the disc is fuelled by the remaining gas that has sunk

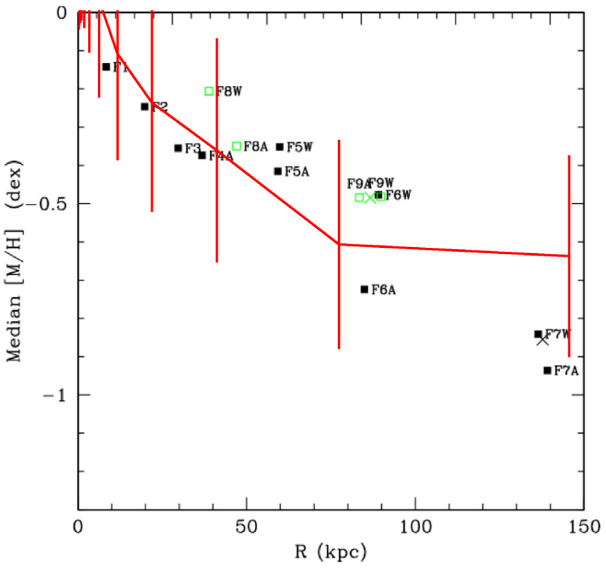

Figure 8. Comparing the mean metallicity gradient between Model-6 (red line) and observation data from Rejkuba et al. (2014) (points). The red line is the mean value for each bin, and the error bars show the scatter of metallicity in each bin in the model.

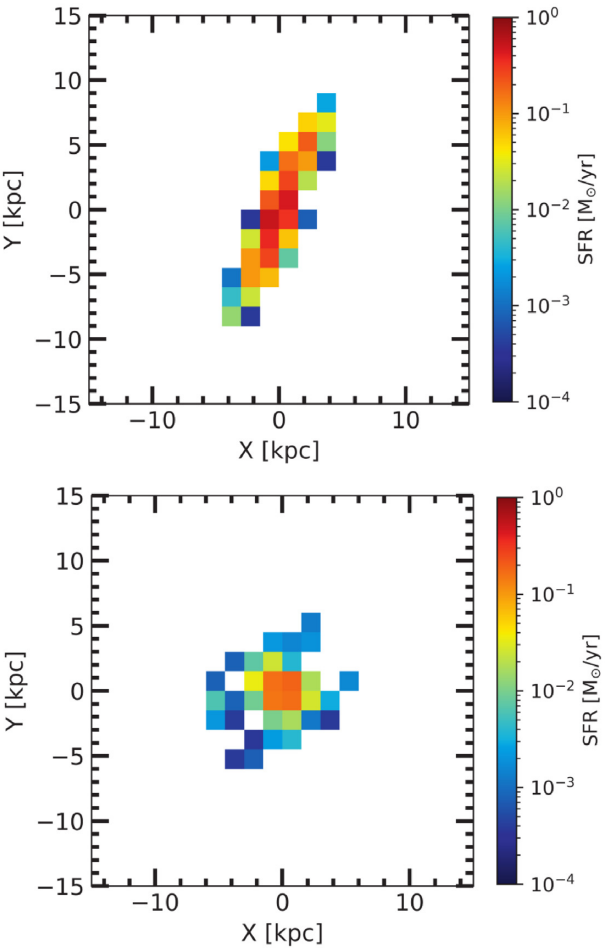

Figure 9. The star formation map of Model-11 is shown in the top panel and Model-6 map is in the bottom panel.

to the centre after the merger ended ∼2 Gyr ago. The total SFRs estimated for Model-6, -11, -7, and Model-10 are 0.85, 3.5, 1.3, and 0.6 M yr^{-1}, respectively. A recent study by Espada et al. (2019) using ALMA CO (1–0) observations produced high-angular resolution (1 arcsec) maps towards the dust lane of Cen A. They found a total molecular gas mass of 1.6×10^9 M , which is higher than that previously measured, and derived an SFR of ∼1 M yr^{-1}. This is remarkably similar to the values we estimate from our simulations. The ALMA map has a much higher resolution and shows a more structured distribution of SFR surface density than can be inferred from the present simulations. It presents a peak in the central circumnuclear disc, which is reminiscent of what we see in Model-6, albeit on a much smaller spatial scale.

5 DISCUSSION AND CONCLUSION

We presented the first hydrodynamical simulations tailored to model the nearest gE Cen A, assuming a major merger with a mass ratio of up to 1.5. From our modelling, the merger event happened ∼6 Gyr ago with the first passage at ∼5 Gyr ago and the fusion of the two progenitors completing 2 Gyr ago. The age distribution of the stars brought in by the progenitors and formed during the merger event is consistent with the stellar age distribution in the halo (Rejkuba et al. 2011). With low gas fractions (20–40 per cent) in the progenitors and a small mass ratio (≤1.5), the merger remnant stellar mass distribution follows a de Vaucouleurs profile, consistent with observations (Dufour et al. 1979).

In the current model, the halo region is dominated by stars coming from the progenitors of the major merger. The two progenitors have been assumed to be massive spirals, so it is expected that relatively metal-rich stars spread throughout the halo region. This may explain the observations showing the relatively high average metallicity of halo stars [M/H] > -1 (Harris & Harris 2000, 2002; Rejkuba et al. 2005) and the shallow metallicity gradient (Rejkuba et al. 2014).

Malin (1978) and Malin, Quinn & Graham (1983) reported the discovery of many faint narrow stellar shells surrounding Cen A. Additional shells in the inner parts of the galaxy were uncovered by Peng et al. (2002), who applied the unsharp masking technique to CCD images of Cen A. Such faint shells and filaments were found to be quite common features of many nearby ETGs (Malin & Carter 1980). There are two principal scenarios in the literature explaining the shell formation. One assumes accretion of a smaller (spiral) galaxy on to an elliptical. Quinn (1984) showed that shells can be formed by the 'phase wrapping' of dynamically cold material with accreted companion on radial orbit. The shells can also be created by 'spatial wrapping' of debris from thin disc (Dupraz & Combes 1986; Hernquist & Quinn 1988). The second scenario proposed by Hernquist & Spergel (1992) assumes a major merger of two equal-mass spirals that results in an elliptical with shells. This scenario solves many difficulties with the shell formation in the minor merger model. In a recent study of the incidence and formation processes of shell galaxies based on the Illustris hydrodynamic cosmological simulation, Pop et al. (2018) reported that shell galaxies observed at $z = 0$ preferentially formed through mergers with relatively major merger ($\gtrsim 1:10$ in stellar mass ratio). Our current work where shells are result of a major merger is consistent with the latter scenario, and also in agreement with recent simulations by Bekki et al. (2003) and Bekki & Peng (2006).

Our modelling has some limitations and does not provide a detailed description of all the observed Cen A properties. For example, the simulated residuals that mostly lie along the main galaxy axis occupy a larger area than that found in observations, and not all the geometrical angles are reproduced together. Some improvements are expected either from observations, e.g. a more accurate determination of stream distances, or from modelling, e.g. by fine-tuning parameters and also by considering different baryonic fractions.

However, the success in modelling Cen A's properties indicates that there are still giant elliptical galaxies that are formed through major mergers in the last few Gyr. The role of major and minor mergers in the mass assembly of massive spiral and elliptical galaxies had been vastly discussed during the last decades. Due to their lower impact and their longer duration (Jiang et al. 2008), minor mergers are considerably less efficient to activate a starburst, and to distort morphologies and kinematics, or they do it in a somewhat sporadic way (Hopkins et al. 2008). On the other hand, the argument can be counter balanced if dwarf galaxies are as numerous as predicted by CDM cosmological models. Observations of moderately distant galaxies ($z_{\rm median} = 0.65$) have revealed that 6 Gyr ago, mass ratio < 5 mergers were quite common (Hammer et al. 2005; Hopkins et al. 2008; Hammer et al. 2009) and similar to expectations from CDM (Puech et al. 2012).

The above could make both M31 and Cen A exceptional since they have experienced a much more recent major merger, about 2 Gyr ago. This also implies a quite efficient mass assembly through mergers in the Local Universe, an evidence that could be further supported if M81 is likely to experience soon a merger with M82 (Smercina et al. 2019).

Perhaps even more intriguingly, Müller et al. (2018, 2019) showed that dwarf galaxy satellites surrounding Cen A are corotating within a gigantic thin plane that has a measured rms height of 133 kpc and a semimajor axis length of 327 kpc. Woodley (2006) compared the kinematics from ∼340 Cen A GCs with over 60 satellite members of Cen A and nearby M83, finding similarities in rotation amplitude, rotation axis, and velocity dispersion between the halo of Cen A and the Centaurus group as a whole. The plane of satellites reported in Müller et al. (2018) is aligned with the galaxy major axis and satellites on the north-east side of Cen A are approaching, while those on the south-west side are receding, indicating a coherent rotation in the same direction as PNe (see fig. 1 in Müller et al. 2018). M31 shares a similar alignment of the gigantic plane with the Giant Stream (Hammer et al. 2013, 2018), and both planes are aligned with the line of sight. Such gigantic plane structures are not well understood in CDM cosmology (Pawlowski et al. 2014), which calls for further observational and simulation studies of Cen A and its dSph satellites.

ACKNOWLEDGEMENTS

The authors thank the referee for helpful suggestions. The computing task was carried out on the HPC cluster at China National Astronomical Data Center (NADC). NADC is a National Science and Technology Innovation Base hosted at National Astronomical Observatories, Chinese Academy of Sciences. This work has been supported by the China–France International Associated Laboratory 'Origins'. Research by DC is supported by NSF grant AST-1814208.

DATA AVAILABILITY

The data underlying this article will be shared on reasonable request to the corresponding author.

REFERENCES

Arnold J. A., Romanowsky A. J., Brodie J. P., Chomiuk L., Spitler L. R., Strader J., Benson A. J., Forbes D. A., 2011, ApJ, 736, L26

Baade W., Minkowski R., 1954, ApJ, 119, 215
Baumschlager B., Hensler G., Steyrleithner P., Recchi S., 2019, MNRAS, 483, 5315
Beasley M. A., Harris W. E., Harris G. L. H., Forbes D. A., 2003, MNRAS, 340, 341
Beasley M. A., Bridges T., Peng E., Harris W. E., Harris G. L. H., Forbes D. A., Mackie G., 2008, MNRAS, 386, 1443
Bekki K., Peng E. W., 2006, MNRAS, 370, 1737
Bekki K., Harris W. E., Harris G. L. H., 2003, MNRAS, 338, 587
Bell E. F., de Jong R. S., 2001, ApJ, 550, 212
Bell E. F., McIntosh D. H., Katz N., Weinberg M. D., 2003, ApJS, 149, 289
Bird S. A., Flynn C., Harris W. E., Valtonen M., 2015, A&A, 575, A72
Carrera R. et al., 2019, A&A, 623, A80
Charmandaris V., Combes F., van der Hulst J. M., 2000, A&A, 356, L1
Cox T. J., Jonsson P., Primack J. R., Somerville R. S., 2006, MNRAS, 373, 1013
Crnojević D., Ferguson A. M. N., Irwin M. J., Bernard E. J., Arimoto N., Jablonka P., Kobayashi C., 2013, MNRAS, 432, 832
Crnojević D. et al., 2016, ApJ, 823, 19
Crnojević D. et al., 2019, ApJ, 872, 80
Daddi E. et al., 2005, ApJ, 626, 680
Dufour R. J., van den Bergh S., Harvel C. A., Martins D. H., Schiffer F. H., Talbot R. J., Talent D. L., Wells D. C., 1979, AJ, 84, 284
Dupraz C., Combes F., 1986, A&A, 166, 53
Ebneter K., Balick B., 1983, PASP, 95, 675
Eckart A., Cameron M., Genzel R., Jackson J. M., Rothermel H., Stutzki J., Rydbeck G., Wiklind T., 1990, ApJ, 365, 522
Espada D. et al., 2019, ApJ, 887, 88
Fall S. M., Romanowsky A. J., 2018, ApJ, 868, 133
Fouquet S., Hammer F., Yang Y., Puech M., Flores H., 2012, MNRAS, 427, 1769
Friel E. D., 1995, ARA&A, 33, 381
Graham J. A., 1979, ApJ, 232, 60
Graham J. A., 1998, ApJ, 502, 245
Hammer F., Flores H., Elbaz D., Zheng X. Z., Liang Y. C., Cesarsky C., 2005, A&A, 430, 115
Hammer F., Flores H., Puech M., Yang Y. B., Athanassoula E., Rodrigues M., Delgado R., 2009, A&A, 507, 1313
Hammer F., Yang Y. B., Wang J. L., Puech M., Flores H., Fouquet S., 2010, ApJ, 725, 542
Hammer F., Yang Y., Fouquet S., Pawlowski M. S., Kroupa P., Puech M., Flores H., Wang J., 2013, MNRAS, 431, 3543
Hammer F., Yang Y. B., Wang J. L., Ibata R., Flores H., Puech M., 2018, MNRAS, 475, 2754
Harris G. L. H., 2010, Publ. Astron. Soc. Aust., 27, 475
Harris G. L. H., Harris W. E., 2000, AJ, 120, 2423
Harris W. E., Harris G. L. H., 2002, AJ, 123, 3108
Harris G. L. H., Harris W. E., Poole G. B., 1999, AJ, 117, 855
Harris G. L. H., Rejkuba M., Harris W. E., 2010, Publ. Astron. Soc. Aust., 27, 457
Hernquist L., Quinn P. J., 1988, ApJ, 331, 682
Hernquist L., Spergel D. N., 1992, ApJ, 399, L117
Hopkins P. F., 2015, MNRAS, 450, 53
Hopkins P. F., Hernquist L., Cox T. J., Younger J. D., Besla G., 2008, ApJ, 688, 757
Hopkins P. F., Cox T. J., Younger J. D., Hernquist L., 2009, ApJ, 691, 1168
Hopkins P. F. et al., 2010, ApJ, 715, 202
Hubble E. P., 1936, Realm of the Nebulae, Yale University Press, New Haven
Hui X., Ford H. C., Freeman K. C., Dopita M. A., 1995, ApJ, 449, 592
Ibata R., Martin N. F., Irwin M., Chapman S., Ferguson A. M. N., Lewis G. F., McConnachie A. W., 2007, ApJ, 671, 1591
Ibata R. A. et al., 2013, Nature, 493, 62
Iodice E. et al., 2017, ApJ, 839, 21
Israel F. P., 1998, A&AR, 8, 237
Jiang C. Y., Jing Y. P., Faltenbacher A., Lin W. P., Li C., 2008, ApJ, 675, 1095
Kainulainen J. T. et al., 2009, A&A, 502, L5
Karachentsev I. D. et al., 2007, AJ, 133, 504
Katz N., Weinberg D. H., Hernquist L., 1996, ApJS, 105, 19
Kaviraj S., Ferreras I., Yoon S. J., Yi S. K., 2005, A&A, 439, 913
Kraft R. P., Vázquez S. E., Forman W. R., Jones C., Murray S. S., Hardcastle M. J., Worrall D. M., Churazov E., 2003, ApJ, 592, 129
Kroupa P., Pawlowski M., Milgrom M., 2012, Int. J. Mod. Phys. D, 21, 1230003
Malin D. F., 1978, Nature, 276, 591
Malin D. F., Carter D., 1980, Nature, 285, 643
Malin D. F., Quinn P. J., Graham J. A., 1983, ApJ, 272, L5
Mathieu A., Dejonghe H., Hui X., 1996, A&A, 309, 30
Metz M., Kroupa P., 2007, MNRAS, 376, 387
Minniti D., Rejkuba M., Funes J. G., Kennicutt R. C., Jr, 2004, ApJ, 612, 215
Mirabel I. F. et al., 1999, A&A, 341, 667
Moellenhoff C., 1979, A&A, 77, 141
Morganti R., 2010, Publ. Astron. Soc. Aust., 27, 463
Mould J. R. et al., 2000, ApJ, 536, 266
Müller O., Pawlowski M. S., Jerjen H., Lelli F., 2018, Science, 359, 534
Müller O., Rejkuba M., Pawlowski M. S., Ibata R., Lelli F., Hilker M., Jerjen H., 2019, A&A, 629, A18
Naab T., Ostriker J. P., 2017, ARA&A, 55, 59
Neff S. G., Eilek J. A., Owen F. N., 2015, ApJ, 802, 88
Oosterloo T. A., Morganti R., 2005, A&A, 429, 469
Oser L., Ostriker J. P., Naab T., Johansson P. H., Burkert A., 2010, ApJ, 725, 2312
Parkin T. J. et al., 2012, MNRAS, 422, 2291
Pawlowski M. S. et al., 2014, MNRAS, 442, 2362
Peng E. W., Ford H. C., Freeman K. C., White R. L., 2002, AJ, 124, 3144
Peng E. W., Ford H. C., Freeman K. C., 2004a, ApJ, 602, 705
Peng E. W., Ford H. C., Freeman K. C., 2004b, ApJ, 602, 685
Ploeckinger S., Recchi S., Hensler G., Kroupa P., 2015, MNRAS, 447, 2512
Pop A.-R., Pillepich A., Amorisco N. C., Hernquist L., 2018, MNRAS, 480, 1715
Puech M., Hammer F., Hopkins P. F., Athanassoula E., Flores H., Rodrigues M., Wang J. L., Yang Y. B., 2012, ApJ, 753, 128
Pulsoni C., Gerhard O., Arnaboldi M., Pillepich A., Nelson D., Hernquist L., Springel V., 2020, preprint (arXiv:2004.13042)
Quillen A. C., de Zeeuw P. T., Phinney E. S., Phillips T. G., 1992, ApJ, 391, 121
Quillen A. C., Graham J. R., Frogel J. A., 1993, ApJ, 412, 550
Quillen A. C., Brookes M. H., Keene J., Stern D., Lawrence C. R., Werner M. W., 2006, ApJ, 645, 1092
Quillen A. C. et al., 2008, MNRAS, 384, 1469
Quillen A. C., Neumayer N., Oosterloo T., Espada D., 2010, Publ. Astron. Soc. Aust., 27, 396
Quinn P. J., 1984, ApJ, 279, 596
Rejkuba M., Minniti D., Silva D. R., Bedding T. R., 2001, A&A, 379, 781
Rejkuba M., Minniti D., Courbin F., Silva D. R., 2002, ApJ, 564, 688
Rejkuba M., Greggio L., Harris W. E., Harris G. L. H., Peng E. W., 2005, ApJ, 631, 262
Rejkuba M., Harris W. E., Greggio L., Harris G. L. H., 2011, A&A, 526, A123
Rejkuba M., Harris W. E., Greggio L., Harris G. L. H., Jerjen H., Gonzalez O. A., 2014, ApJ, 791, L2
Romanowsky A. J., Fall S. M., 2012, ApJS, 203, 17
Salomé Q., Salomé P., Combes F., Hamer S., 2016a, A&A, 595, A65
Salomé Q., Salomé P., Combes F., Hamer S., Heywood I., 2016b, A&A, 586, A45
Samurovic S., 2006, Serb. Astron. J., 173, 35
Santoro F., Oonk J. B. R., Morganti R., Oosterloo T. A., Tadhunter C., 2016, A&A, 590, A37
Sarajedini A., Jablonka P., 2005, AJ, 130, 1627
Sauvaget T., Hammer F., Puech M., Yang Y. B., Flores H., Rodrigues M., 2018, MNRAS, 473, 2521
Schiminovich D., van Gorkom J. H., van der Hulst J. M., Kasow S., 1994, ApJ, 423, L101
Sersic J. L., 1958, The Observatory, 78, 24
Skrutskie M. F. et al., 2006, AJ, 131, 1163
Smercina A. et al., 2019, preprint (arXiv:1910.14672)
Struve C., Oosterloo T. A., Morganti R., Saripalli L., 2010, A&A, 515, A67

Taylor M. A., Puzia T. H., Muñoz R. P., Mieske S., Lançon A., Zhang H., Eigenthaler P., Bovill M. S., 2017, MNRAS, 469, 3444
Tingay S. J. et al., 1998, AJ, 115, 960
Toomre A., Toomre J., 1972, ApJ, 178, 623
van den Bergh S., 1976, ApJ, 208, 673
van der Kruit P. C., 2007, A&A, 466, 883
van Gorkom J. H., van der Hulst J. M., Haschick A. D., Tubbs A. D., 1990, AJ, 99, 1781
Voggel K. T., , Seth A. C., Sand D. J., Hughes A., Strader J., Crnojevic D., Caldwell N., 2020, ApJ, 899, 140
Walsh J. R., Rejkuba M., Walton N. A., 2015, A&A, 574, A109
Wang J., Hammer F., Athanassoula E., Puech M., Yang Y., Flores H., 2012, A&A, 538, A121
Wang J., Hammer F., Puech M., Yang Y., Flores H., 2015, MNRAS, 452, 3551
Wang J., Hammer F., Yang Y., Ripepi V., Cioni M.-R. L., Puech M., Flores H., 2019, MNRAS, 486, 5907
Wild W., Eckart A., 2000, A&A, 359, 483
Wilkinson A., Sharples R. M., Fosbury R. A. E., Wallace P. T., 1986, MNRAS, 218, 297
Woodley K. A., 2006, AJ, 132, 2424
Woodley K. A., Harris W. E., Beasley M. A., Peng E. W., Bridges T. J., Forbes D. A., Harris G. L. H., 2007, AJ, 134, 494
Woodley K. A., Gómez M., Harris W. E., Geisler D., Harris G. L. H., 2010a, AJ, 139, 1871
Woodley K. A., Harris W. E., Puzia T. H., Gómez M., Harris G. L. H., Geisler D., 2010b, ApJ, 708, 1335
Wu H., Cao C., Hao C.-N., Liu F.-S., Wang J.-L., Xia X.-Y., Deng Z.-G., Young C. K.-S., 2005, ApJ, 632, L79
Yang Y., Hammer F., Fouquet S., Flores H., Puech M., Pawlowski M. S., Kroupa P., 2014, MNRAS, 442, 2419
Zoccali M. et al., 2017, A&A, 599, A12

This paper has been typeset from a TEX/LATEX file prepared by the author.